JMEPEG
https://doi.org/10.1007/s11665-024-10182-6

1059-9495/$19.00

ORIGINAL RESEARCH ARTICLE

Revisiting the Effect of Casting Thickness and Austempering Temperature of Gray Iron

Kamran Kaboli, Meisam Mostafapour, N. Kheirkhahan, E. Edalati, E. Solbi, A. Babakhani, and A.R. Kiani-Rashid

Submitted: 19 May 2024 / Revised: 30 June 2024 / Accepted: 19 July 2024

In the current research the role of sample's thickness and subsequent imposed cooling rate differences has been investigated for gray cast iron in conjunction with revealing the effect of change in austempering temperature. Rectangular and wedge-shaped specimens were cut from casted bulk and subjected to an austenitizing temperature of 900 °C. In the case of the rectangular samples, austempering temperatures of 380, 400, and 420 °C were employed, while the wedge-shaped specimens underwent at a constant temperature of 400 °C. The wedge-shaped specimens were employed to investigate variations in section size. Distinct graphite flake morphologies (A-D) emerged, contingent on section size and cooling rate. Microstructural characterization encompassed optical microscopy (OM), scanning electron microscopy (SEM), and scanning tunneling microscopy (STM). To assess the impact of heat treatment on mechanical properties, hardness tests and Charpy impact tests were executed. It was observed that austempering increased toughness while resulting in decreased hardness values with higher austempering temperatures. The correlation between the simulated model and experimental data affirmed the pivotal role of thickness in augmenting hardness.

Keywords austempering, bainitic, gray cast iron, hardness, microstructure, scanning tunneling microscopy (STM)

1. Introduction

Gray cast iron (GCI or GI), also recognized as flake or lamellar graphite cast iron, is an industrial predominant branch of cast iron alloys; the typical microstructure includes flake graphite in a matrix of pearlite and ferrite. This type of cast iron could be classified as the Fe-C-Si alloy family containing a tiny amount of alloy elements. GCI has produced annually about 50 million tones worldwide (Ref 1, 2).

Among all other types of cast iron, flaky shape of graphite in GCI creates vast potential application for use it in such industrial utilizations in valves, flanges, pipe fittings, or machine tool bases due to its outstanding damping properties. It also displays a suitable wear resistance property combined with good machinability and excellent castability for fabrication of complex shapes (Ref 3-6).

Cooling rate and carbon equivalent are two leading indicators in predicting favor formation of GCI or white iron where lower cooling rate or higher carbon equivalent promotes the final microstructure of GCI (Ref 3, 7).

Jabbari Behnam et al. concluded that the cooling rate significantly affects primary dendrite arm spacing (PDAS), secondary dendrite arm spacing (SDAS), ferrite–cementite layer thickness, and subsequently, hardness (Ref 8). Recently, Lei Ji et al. explored the effect of cooling rate in stepped specimens and concluded the PDAS and SDAS refining by higher cooling rate in thinner stairs (Ref 9). Shahla and Haque emphasized that microstructure characteristic changes significantly by different solidification rates due to high and low heat flow through the mold (Ref 10).

Based on ASTM-A247, there are five different distributions for flaky graphite in GCI which are further classified by their size (Ref 11). However, several studies have been done to correlate two factors of solidification time and cooling rate with the mechanical properties of GCI (Ref 12, 13). According to previous studies, one may assume that different section size leads to different cooling rate (Ref 5, 11, 12). The cooling rate can immensely affect the morphology and shape of formed flaky graphite in GCI and subsequently causes various properties such as increase in the hardness (Ref 14-16) and also get higher tensile and bending properties (Ref 10) in accelerated cooling rates. Graphite inhabits different mechan-

Supplementary Information The online version contains supplementary material available at https://doi.org/10.1007/s11665-024-10182-6.

Kamran Kaboli, Department of Metallurgical and Materials Engineering, Faculty of Engineering, Ferdowsi University of Mashhad, P.O. Box 91775-1111, Mashhad, Iran; and Key Laboratory for Advanced Materials of Ministry of Education, School of Materials Science and Engineering, Tsinghua University, Beijing 100084, China; **Meisam Mostafapour**, Department of Metallurgical and Materials Engineering, Faculty of Engineering, Ferdowsi University of Mashhad, P.O. Box 91775-1111, Mashhad, Iran; and School of Metallurgy and Materials Engineering, College of Engineering, University of Tehran, Tehran, Iran; **N. Kheirkhahan**, Department of Metallurgical and Materials Engineering, Faculty of Engineering, Ferdowsi University of Mashhad, P.O. Box 91775-1111, Mashhad, Iran; and Dipartimento Interateneo di Fisica, Universita di Bari, 70126 Bari, Italy; **E. Edalati, A. Babakhani,** and **A.R. Kiani-Rashid**, Department of Metallurgical and Materials Engineering, Faculty of Engineering, Ferdowsi University of Mashhad, P.O. Box 91775-1111, Mashhad, Iran; and **E. Solbi**, School of Metallurgy and Materials Engineering, College of Engineering, University of Tehran, Tehran, Iran. Contact e-mail: k_kaboli_m@yahoo.com.

Published online: 01 October 2024

ical properties for the whole system governed by distribution, size, morphology, and amount of graphite phase (Ref 8). Similar to study conducted by Kiani-Rahid et al., Sahu et al. also showed that the thin to thick section size of staircase sample could lead to smaller and larger graphite flake sizes, respectively. Actually, with a sharp undercooling, improper dissipation of graphite can happen beside elements segregation. So, the inhomogeneity seems to be an inevitable phenomenon in a thinner section due to their relatively high cooling rate. This issue established a contradictory trend for hardness measurement where higher hardness can be expected in thin sections and lower hardness would be waited for thick sections (Ref 14, 15).

The austempering procedure orchestrates a transformative sequence wherein ferrite plates (α) initiate and propagate within the primary austenite grain (γo), demarcated by slender strata of high carbon austenite (γHC). As the reaction advances, the carbon diffusion process progressively encounters hindrances, culminating in the cessation of ferrite plate expansion. The residual austenite assumes stability through heightened carbon content, thereby enabling controlled cooling to ambient temperature sans martensitic transformation. This controlled treatment engenders a distinctive microstructural composition marked by stable austenite and acicular ferrite phases, commonly referred to as ausferrite. The austempering process usually includes austenitizing at the temperature range of 840-900 °C for 1 h or more according to the structure and thickness of the as-cast piece and then conducting the austempering process at the temperature range of 230-450 °C. By increasing holding time in austempering process, high carbon austenite undergoes bainite transformation through formation of ferrite and precipitation of cementite particles; this bainitic structure causes desirable wear resistance, fracture toughness, vibration, and sound damping (Ref 17-19).

Considering bainite transformation as a global phenomenon for austempered gray iron (AGI) and austempered ductile iron (ADI), it can be categorized into two distinct stages with two different products entitled lath-like lower bainite and feather-like upper bainite. Proceeding in this stage enables further transformation of carbon-enriched austenite to bainite and epsilon carbides by holding at relatively high austempering temperatures. Meanwhile, the bainitic ferrite which is the product of austempering heat treatment in the early stages and relatively high austempering temperatures inherited the morphology so close to upper bainite. It can be formed just before completion of whole process of bainitic transformation. Hereafter, the upper bainite in this text means the shape of bainitic ferrite (Ref 2). For ADI, it is accepted that upper bainite forms with the successive and isothermal formation of bainite subunits at temperatures above 330 °C (Ref 20). At higher austempering temperatures, the first transformation product comes from microstructural evolution consisting of bainite platelets having high carbon austenite between them (Ref 17). The high percentage of carbon is rejected in the austenite by nucleation and growth of low carbon bainite ferrite (Ref 15). However, the metastable, high-carbon austenite will transform to ferrite and carbide in the final stage of transformation by prolonging austempering times (Ref 19). Upper bainite-shaped bainitic ferrite was studied in the present study, and due to the higher formation temperature in the upper bainite stage compared with the lower bainite stage, carbon rejection from bainitic ferrite to austenite happens more rapidly. Carbon-enriched austenite in this level exhibits lower martensite start temperature, and its thermal stability increased enormously. With initially interrupting at austempering temperature, it is anticipated to have some martensite in cooled samples, which may be due to incomplete bainite transformation (Ref 21). In the case of containing high silicon in the range of 1-2wt.% or aluminum addition in the nominal composition of cast iron, carbide precipitation is highly prevented during the process of upper bainite-shaped bainitic ferrite formation. Eventually, the final microstructure mainly consists of retained austenite, graphite, bainitic ferrite, and probable martensite, which can be transformed from austenite upon cooling from a relatively high austempering temperature (Ref 2, 3, 21-26). Austempered gray cast iron (AGI) is a strategically designed composite material characterized by its remarkable wear resistance and commendable mechanical properties, prominently highlighted by elevated tensile and fatigue strength, coupled with favorable ductility and impact resistance attributes (Ref 23-28).

Seikh et al. introduced a copper-containing austempered gray iron (AGI) with a lower corrosion rate. They indicated a specific microstructure consisting of austenite and bainitic ferrite called ausferrite that could enhance the corrosion resistance of AGI (Ref 28). Balachandran et al. emphasized the magnificent wear resistance of AGI compared with other heat treatment processes (Ref 29). In a recent study, Wang et al. suggested a laser hardening treatment on AGI samples to reveal desirable high wear resistance (Ref 30). In another study, Sarkar and Sutradhar also showed that tribological properties of a copper enriched GCI can improve by austempering process (Ref 31). But the effect of thickness variation on AGI is worth to study in more detail.

It is accepted that mechanical properties of austempered cast iron strongly correlated with austempering time and temperature, which affect microstructure morphology, the amount of carbon in the austenite phase, and volume fraction of retained austenite (Ref 31). Studies accentuated the effect of austempering temperature in the mechanical properties and microstructural characterization of ADI (Ref 32, 33). AGI also needs to get more attention in academic society mainly due to the maximum production of GCI compared with its counterparts (Ref 1). It is well accepted that the AGI and conventional GI mostly use as a base material for desired significant wear or damping properties (Ref 8, 9, 17-19), but fatigue strength is another aspect which is directly related to the microstructural characteristic of cast iron. While there are enormous number of papers about fatigue behavior of ductile cast iron (Ref 34-36), it seems that the role of microstructure and bainitic products in fatigue strength is worth to work also in the future research.

Despite many reliable and deep published articles about the role of austempering in the impact energy enhancement of austempered ductile iron (ADI) (Ref 36-42), such investigation is rare for AGI (Ref 43). It has already been proven that increased austenitizing temperature effects on the saturation of austenite by diffusion of carbon from the neighboring graphite and promotes lower bainite formation through austempering heat treatment (Ref 3). Likewise, Gundlach studied the role of Mn on mechanical properties of cast iron (Ref 25); meanwhile, Blackmore and his colleague believe that carbide former elements such as Mn and Mo segregate during solidification. They claim that Mn and Mo can concentrate on eutectic cell boundaries, decreasing elongation and toughness in as-cast pieces. Evidence shows that the growth of bainitic ferrite and subsequent bainite without carbide makes the austenite carbon-filled (Ref 44). The inter-dendritic carbide can form where Mo

content is higher than 0.5 wt.%, known as a brittle constituent (Ref 3).

Ni element as an austenite stabilizer can diminish carbon diffusion into austenite and promote feathered like upper bainite in bainitic ferrite formation (Ref 14). Some authors confirmed the effect of Ni on enhancing the hardness and toughness of cast iron by actuating solution strengthening effect via carbon atoms (Ref 45, 46). So, chemical composition, austenitizing temperature–time, austempering temperature–time, and critical temperatures should be carefully selected if the upper bainite formation is intended as a target (Ref 47).

To the best of our knowledge, contrary to the large amount of published research on ADI, reliable research studies on AGI require more consideration. So, the aim of this research is to investigate the effect of section size variation on simulated as cast and AGI by introducing related equations for heat flow during solidification. The applied characterization techniques in the current study can shed light for more artistic imaging of the bainitic ferrite microconstituent for future researchers with reasonable phase tracing. A detailed description also demonstrated to reveal the effect of increasing austempering temperature with equal holding time and the related trade-off between microstructural characteristics and the mechanical properties of GCI. So, besides the study of microstructure evolution, a deep microscopy characterization was also utilized using STM microscopy, which is supposed to improve the general understanding of the morphology appearance of the bainite as a complementary characterization technique in the cast iron field.

2. Materials and Methods

In the present study, two types of samples were fabricated as follows:

1- Wedge-shaped samples with dimensions of 127*25.4*44.4 millimeters. (The vertex angle was chosen 32 degrees as per ASTM A367 (Ref 48)).
2- Rectangular cubic-shaped samples with dimensions of 90*30*25 millimeters.

Three molds were fabricated for each wedge-shaped and rectangular cubic-shaped sample using the carbon dioxide method and sodium silicate glue. A 1400 °C melt with chemical composition as shown in Table 1 was provided using an induction furnace and then was cast by pouring into the united sand mold without inoculation. The chemical composition of melt is the outcome of spectroscopy test on final samples (sample are available upon request). The CE calculated using both conventional (Ref 3) and more accurate one, considering the role of wider elements (Ref 7).

Table 1 Chemical composition of the alloys in this study

Sample	Chemical composition, wt.%							
Fe (Bal.)	C	Si	Ni	Mo	Mn	S	P	CE
W-A	3.2	2.4	1	1	0.37	0.04	0.04	4.01 [3] 4.07 [7]

After cooling down to the environment temperature, the casting samples were detached from the molds. Then the gates were separated from them.

According to a method of the chill test described in ASTM A367 (Ref 48), there are three different regions in the as-cast sample affected by cooling rate:

1- GCI region (Region 1).
2- Probable mottled cast iron region (Region 2).
3- Probable white cast iron region (Region 3).

The mentioned regions are illustrated as a schematic in Fig. 1. Three points are also indicated in this figure as A, B, and C, further explained in the next section.

Figure 2 illustrates TTT and CCT curves calculated by JMatPro. The formation of bainite in conjunction of austenite and martensite can be guaranteed even in 1 h of holding time but not complete at designed time. So, according to (Ref 2, 3) and due to relatively high austempering temperature, the upper bainitic shape bainitic ferrite is expected to form through the heat treatment process in this paper.

Wedge-shaped workpieces were austenitized in a resistance furnace at 900 °C for 60 min, followed by quenching in a molten salt bath (Sodium nitrate) as an austempering media with temperature of 400 °C and 60 min as holding time. To just investigate the effect of section size on wedge-shaped samples of GCI, the additional section containing probable mottled and white cast iron was discarded as per Fig. 1.

To examine the effect of austempering temperature, the optimum holding time according to the literature was selected as 60 min (Ref 49). Then, provided rectangular cubic samples were austenitized in the resistance furnace at the temperature of 900 °C maintained for 60mins and subsequent heat treatment cycles were accomplished on them as follows:

R-A, R-B, and R-C were quenched in a molten salt bath with three different austempering temperatures of 380, 400, and 420 °C, respectively, and were held for 60 min. Finally, all samples were cooled in the air.

In order to reveal the role of cooling rate stemmed from section size on microstructural and mechanical characteristics

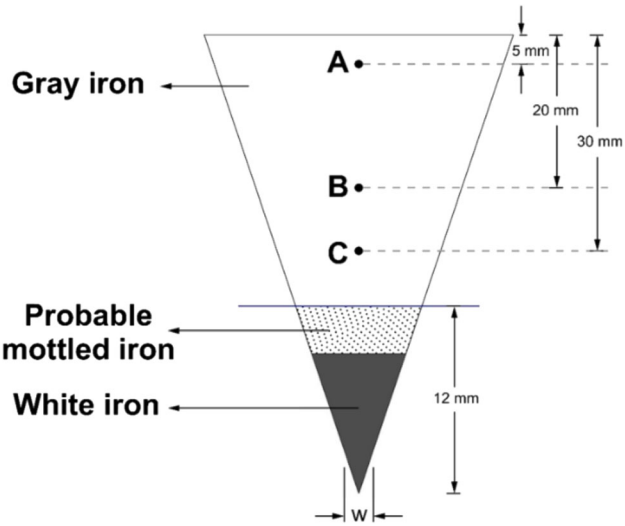

Fig. 1 Schematic figure of wedge-shaped GCI according to ASTM A367

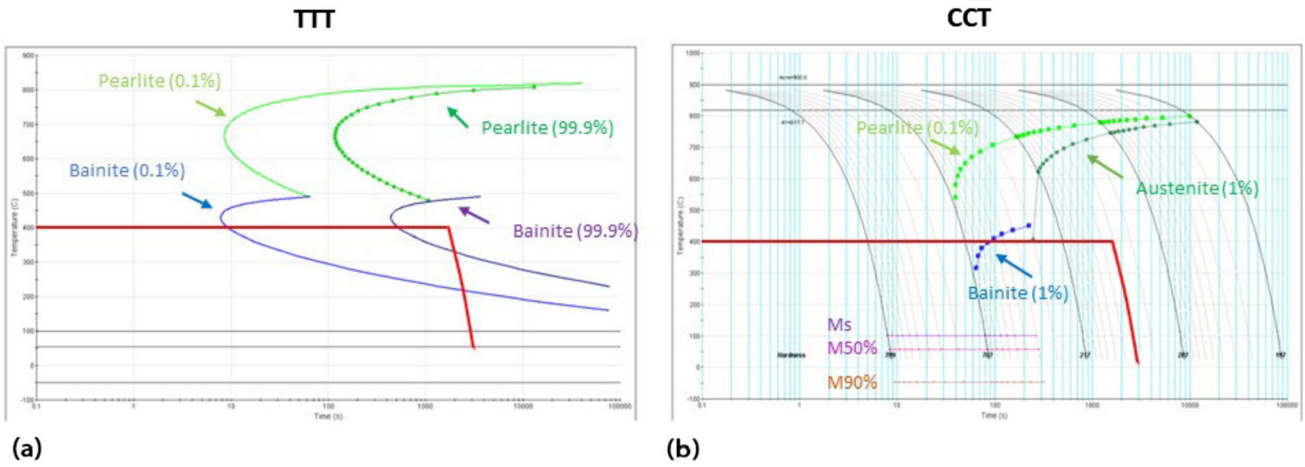

Fig. 2 (a) TTT & (b) CCT curves of tested cast iron

of austempered wedge-shaped samples, microstructural characterization and hardness tests were accomplished on prepared metallography specimens based on ASTM E3 (Standard Guide for Preparation of Metallographic Specimens) (Ref 50). Microscopic examinations were done using an optical microscope, scanning electron microscope (SEM: LEO1450VP), and scanning tunneling microscope (STM: NAMA-STM SS2). Microstructure image processing software (MIP) was applied to measure the fraction of contributed phases.

Metallography specimens were ground using emery paper with grit size range from 60 to 1200. An as-polished specimen was selected for STM imaging which will be explained in Sect. 3.1. Preparing metallography samples was followed by mechanical polishing using Buehler wheel polishing machine with Al_2O_3 as a slurry suspension with particle dimensions of 0.3 and 0.05 μm. Provided specimens were then mounted and prepared for microscopically analysis by etching at 2% Nital etchant for 3 s.

The unnotched Charpy impact test was utilized for determination of the impact toughness of rectangular cubic samples by finishing austempering heat treatment. The experimental tests were conducted at room temperature. Workpieces were provided with standard dimensions of 10*10*55 mm according to ASTM A327 (Ref 51) and trimmed from the middle of samples far enough from mold-contact cooling sides. Related standard is the suggested procedure method for austempered cast irons in previous papers (Ref 52). In addition to microstructural analysis, Vickers hardness test was accomplished a Vickers Engineering Group-Vickers hardness tester equipment at the 50-kg load on the as-polished austempered specimens to investigate the influence of austempering temperature on mechanical properties of AGI. Meanwhile, heat flow methodology of simulated as-cast samples can be found as supplementary material of this article (Ref 53-56).

3. Results and Discussion

3.1 Microstructure Results

The microstructural study was accomplished in A, B, and C points of austempered and trimmed wedge-shaped specimen in x = 25 mm also for the cross-sectional cut in the central area of R-A, R-B, and R-C samples. Figure 3 indicates the microstructure of wedge-shaped samples in three different regions as delineated in the schematic image of Fig. 1. Unetched images were provided from trimmed wedge-shaped samples to depict graphite distribution along with the specimen. As shown in Fig. 3(b) and (c), different thicknesses in specified points of wedge-shaped samples resulted in different kinds of lamellar graphite morphology. The A point contributes to a lower cooling rate mainly due to thick section and A type of randomly oriented graphite distributed in the microstructure according to entitled graphite classes in ASTM A247 (Ref 11). In the B point, the distribution of graphite flakes is affected by relatively thinner section size compared to the A point. Subsequently, there is a lower material amount during solidification or heat treatment to do convection or conduction, respectively. So, B-type graphite is the predominant morphology for this area of GCI region. At the area near the smaller side of the trimmed wedge-shaped sample named C, a combination of D and E graphite types spread over the microstructure of the GCI region, which is related to higher cooling mode due to thin section size. Sundaram believed that both D and E graphite types have interdendritic segregation by solidification and are typical types of graphite distribution in hypo-eutectic cast iron (Ref 57). Despite in mechanically induced graphite flakes in ductile cast iron (Ref 58), graphite formation tendency and its related morphology in thermally fabricated graphite flakes of GCI are controlled by chemical composition, inoculation, undercooling, and cooling rate (Ref 59, 60). High silicon and relatively high Ni amount in the chemical composition of investigated GCI promote graphitization. It may be the reason for not illustrating evidence for mottled regions in the selected C point as a thin section in the trimmed wedge-shaped sample.

It should be noted that austenitizing can induce dissolution of carbides and also carbon diffusion in high saturated austenite. The subsequent holding time in austempering temperature also affects the carbon diffusion from bainitic ferrite to the austenitic matrix. The reasons mentioned above may motivate the nucleation of secondary graphite or changing graphite distribution in the GCI sample. With this fact in mind, graphitization is expected supposedly. Despite that, with the same dimensional sample parameters during austempering heat treatment, no substantial difference was observed for all investigated points along with the wedge-shaped sample.

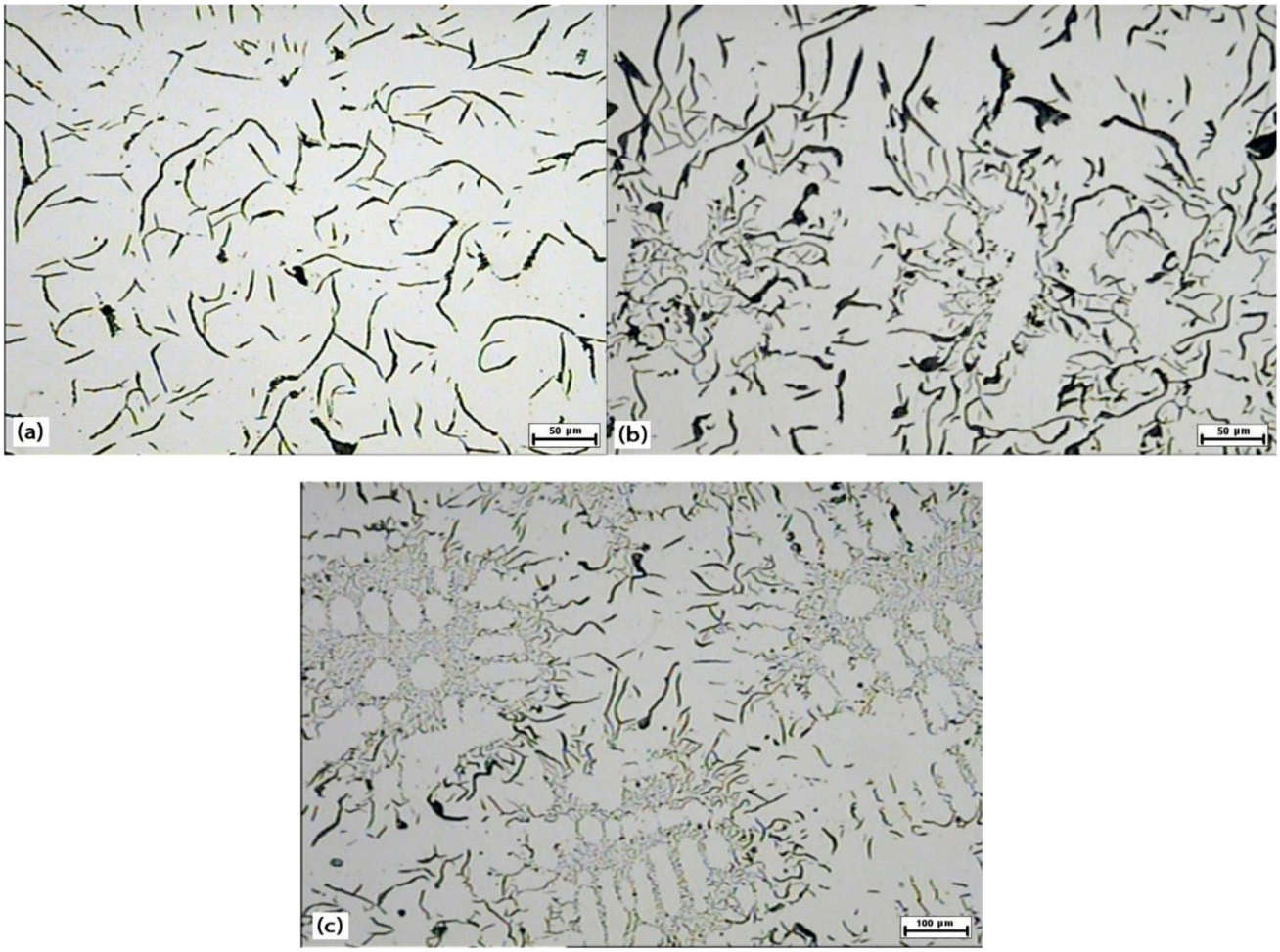

Fig. 3 (a-c) Optical microscopy of unetched specimens of wedge-shaped sample in A, B, and C points, respectively

However, regardless of precaution in cutting sample only in the GCI region, it is a suitable response for not revealing white iron or mottled iron in selected skinny section size.

To precisely study the microstructure of the wedge-shaped sample, prepared metallography specimens were conducted to Nital 2% as an etchant for 3 s. The results are shown in Fig. 4; it is worth mentioning that the processing instruction was according to color etching explained in detail in the Kovac et al. paper (Ref 2). The microstructure consists of graphite, martensite, and bainitic ferrite in a matrix of retained austenite, the resulting microstructure entitled ausferrite. The resulting bainite bainitic ferrite microstructure was categorized as feathery-shaped bainitic ferrite, which was achieved by the relatively high austempering temperature of 400 °C. As observed by increasing section size, the amount of bainitic ferrite microconstituent increases. Meantime, the sheaf in feather shape tends to become stronger and wider. One may consider the relatively high amount of Ni as a reason. Ni element as an austenite stabilizer promotes austenite stability in the matrix. Ni element effects on CCT diagram and pushes it downward, so it may be reasonable to conclude that approximately high Ni in composition leads to coarsening the feather-shaped bainitic ferrite (Ref 14).

From a microstructural viewpoint, it can be grasped that the martensite microstructure in a thin section of C is coarse and extensive which can be seen as a brown bundle, resulting from the high cooling rate due to the low amount of neighboring bulk material and more close chilling sides. A metallography procedure consists of 3 s of immersing in Picral etchant also recruited to reveal the carbide in the microstructure. There was no evidence of carbides in A and B points, thanks to their high enough section size. But by characterization of the C point located in the thin section of the wedge-shaped sample, it seems that the carbide phase was visible mainly in grain boundaries, as shown in Fig. 5(b). Carbide formation consumes the carbon content and makes the austenite to be unstable and more prone to martensite transformation. Observed carbide phase embedded in the retained austenite matrix, which had a hardness value of about 612-882 Vickers and SEM-EDX delineates Mn enriched them. The formation of this phase can be explained by the gathering of carbide stabilizing elements as Mo and Mn in intergranular areas. It is further affected by possibility of having some carbides in the thinner sections with higher cooling rate and higher Ni solution as discussed before. It is accepted reason with the helping of calculation in Scheil solidification feature as indicated in Fig. 5(a). As can be seen, the first product of molten cast iron in the cooling down process forms as austenite at around 1206 °C and proceeds by predicted MnS stability at the temperature of 1196 °C, which can be considered as a reason for element segregation in advance. The Scheil curve prediction shows graphite formation at the temperature of 1167 °C. It was detected that deviation from

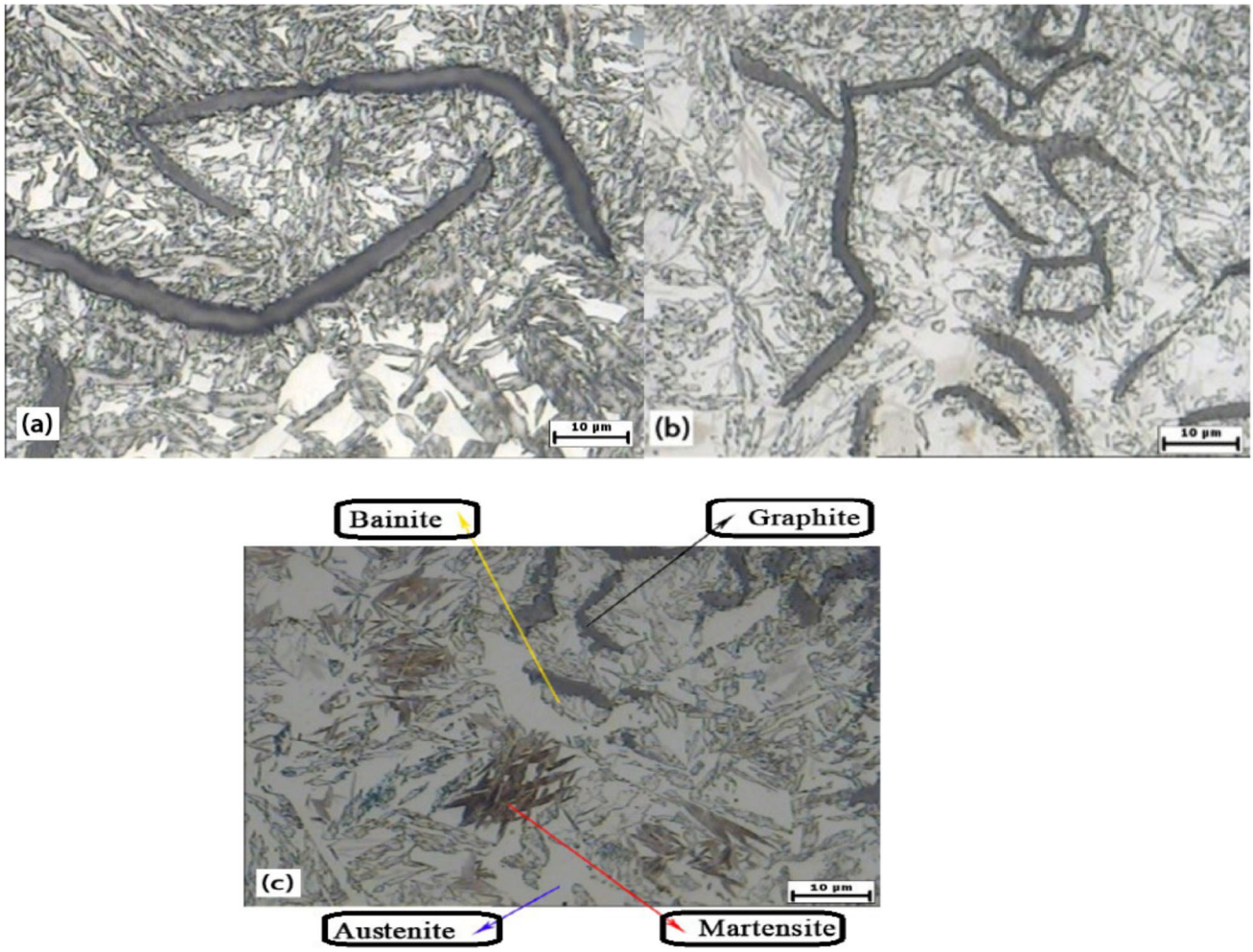

Fig. 4 (a-c) Optical microscopy of etched specimens of wedge-shaped sample. A, B, and C points, respectively, which is according to Fig. 1. The magnification of all samples is in 10 μm (color indication: black: graphite, yellow: bainitic ferrite, red: martensite, blue: austenite)

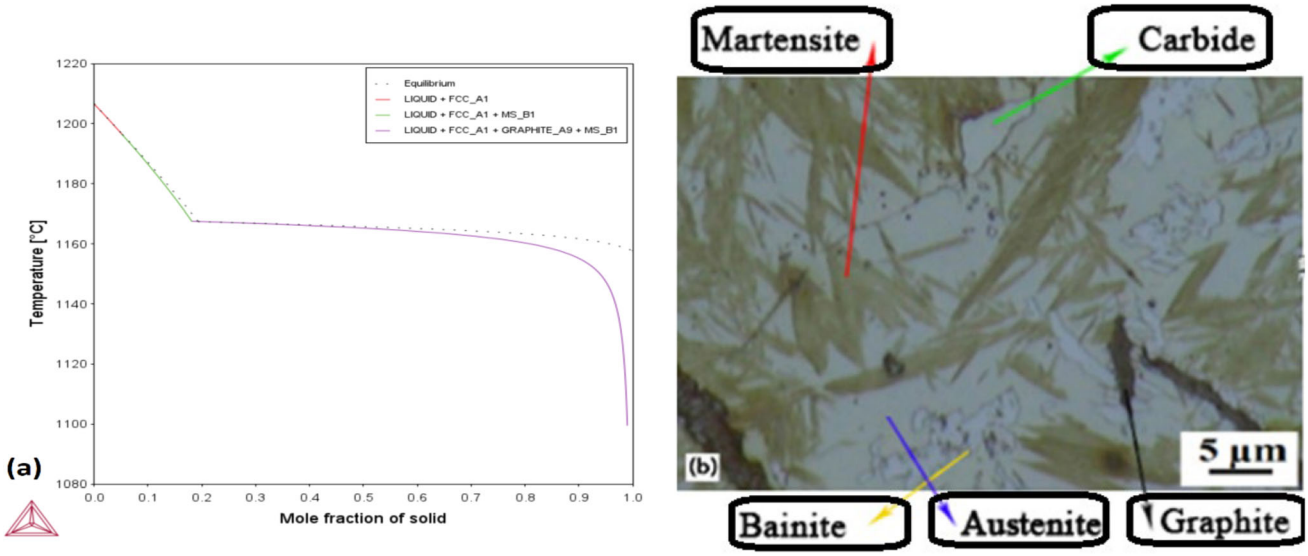

Fig. 5 (a) Forecasting out of equilibrium tendency using Thermo-Calc for current GCI, (b) optical microscopy of Picral etched specimen of wedge-shaped sample in C point (color Indication: black: graphite, yellow: bainitic ferrite, red: martensite, blue: austenite, green: carbide)

the equilibrium state is supposed for cast iron's current chemical composition, which is a micro-segregation actuator.

In a similar characterization technique for rectangular cubic samples, which were austempered at various temperatures, the contribution of phases was calculated using Image Analyzer Software of Clemex and is indicated in Table 2 as an average of three different measurements. The microstructures of etched samples in Nital 2% remained for 3 s are also indicated in Fig. 6. It can be seen that the dominant type of graphite in all three sections is A-type embedded in a matrix of retained austenite with a mixture of bainitic ferrite and martensite as surrounding phases.

An increment in the amount of both bainitic ferrite and retained austenite by subjecting to higher austempering temperature can be concluded as indicated in Table 2. Sarkar et al. also confirmed the attainability of high austenite fraction in the relatively high austenitizing temperature around 900 °C as a first heating treatment (Ref 31). Meanwhile, the martensite fraction reduced abruptly. Increasing austempering temperature can motivate rapid carbon diffusion in the austenitic matrix and thermally stabilize it at room temperature by avoiding martensite transformation in cooling to some extent. In the same way, a higher austempering temperature can induce feather liked bainitic ferrite formation more easily and accentuate its feature shape tendency. It can also cause higher driving force for carbon diffusion, so as much as high austempering temperature as low as martensite fraction is anticipated. Ławrynowicz asserted that in austempered cast iron due to inhomogeneous microstructure in comparison with austempered steel (high carbon content graphite + bainite + ferrite + austenite + …), other products like martensite are also supposed to form just before necessary time for bainite completion and during the bainite formation (Ref 61). Carbide formation in higher cooling rate of thinner sections can also depleted more carbon from austenite and cause higher fraction of martensite as it can be seen in Fig. 5(b). Other researchers also accentuate that extremely segregated elements in cast iron due to presence of graphite and other phases cause it more vulnerable to martensite transformation in cooling form austempering temperature to room temperature, especially in last solidified regions of cast iron melt, e.g., cell boundaries which contain less stable austenite with lower carbon content (Ref 62, 63). Figure 7(a) delineates SEM micrographs for B point of wedge-shaped sample. Figure 7(b) also illustrates the counterpart image for R-A rectangular cubic-shaped GCI with embedded martensite in austenite. It is also evident that bainitic ferrite morphology can be detected clearly by its feather shape.

STM (scanning tunneling microscopy) is characterization process for topological detection by high enough lateral and vertical resolution of about 1 Å. However, despite some published articles helping STM imaging in steels (Ref 14, 64), this kind of microscopy has been neglected up to this time to be recruited in ferrous alloys and cast irons characterization.

In a very first research using scanning tunneling microscopy for steel material, Yang et al. and Fang et al. studied bainite formation using that. They stipulated that bainite morphology can be distinguished by tent-shaped surface relief (Ref 64). Plate-like transformation products are constructed through two different surfaces relying on the invariant plane strain (IPS) or tent-like. The former is related to the shear transformation of martensite with intact habit plane, while later is the undulation characteristic bainite transformation associated with diffusion. Topography results in AFM (atomic force microscopy) and STM (scanning tunneling microscopy) characterization indicated that bainite could be recognized by tent-shaped surface relief and some undulations. But this surface relief is not capable to plastically deform adjacent austenite, hence topographically is visible (Ref 65). Reducing the number of contributed phases is an essential task to avoid any misunderstanding of STM images' interpretation. So, the R-C sample was chosen due to the high amount of retained austenite and carbide-free upper bainite shape of bainitic ferrite microconstituent. It is accepted that bainite nucleation happened in two neighboring phases of austenite or graphite (Ref 3). Nevertheless, the topological characteristics of graphite are too sharp and easy for detection. So, the R-C sample with enough high austempering temperature was selected for the topological study of bainitic ferrite because of a meager amount of unfavored phases regardless of mature feathers like bainitic ferrite, austenite, and inevitable phase of flaky graphite.

Unlike controversial debates on bainite formation, whether it is a military and displacive transformation or diffusional (Ref 3, 65). The authors adopt a displacive mechanism for bainite formation continued by carbide precipitation in upper bainite in typical chemical composition.

In the current study, carbide-free bainitic ferrite is supposed to form through a displacive method, regardless of relatively enough high austempering temperature where yield strength of austenite is diminished (Ref 65). However, the STM image of as-polished sample can be further topologically explained by strain accommodation but not plastically deformation in austenite during bainite formation. It may be due to the likely weaker effect of bainite compared to martensitic transformation. Strain accommodation is initialized by sub-unit and further sub-unit development of lower bainite or feature sheaf coarsening of upper bainite, which causes dislocation accumulation in austenite. The early-stage formation of bainitic ferrite also follows the same. Despite bainitic ferrite illustration using STM image in the previously published work by some of the current authors (Ref 14), the reason behind the topological feature of bainitic ferrite needs more elaboration. To the best of the author's knowledge, it is the first time to characterize the bainitic ferrite microconstituent in cast iron helping scanning

Table 2 Fraction of contributed phases in rectangular cubic samples austempered at 380, 400, and 420 °C and related standard deviation (SD)

Sample	Retained austenite, SD	Bainitic ferrite, SD	Martensite, SD	Flaky graphite, SD
R-A	17.62/0.5	43.26/1.2	15.40/0.1	23.72/0.07
R-B	19.35/1.4	46.20/2.3	12.15/0.08	22.3/0.07
R-C	20.72/0.7	52.5/0.5	4.26/0.9	22.52/0.1

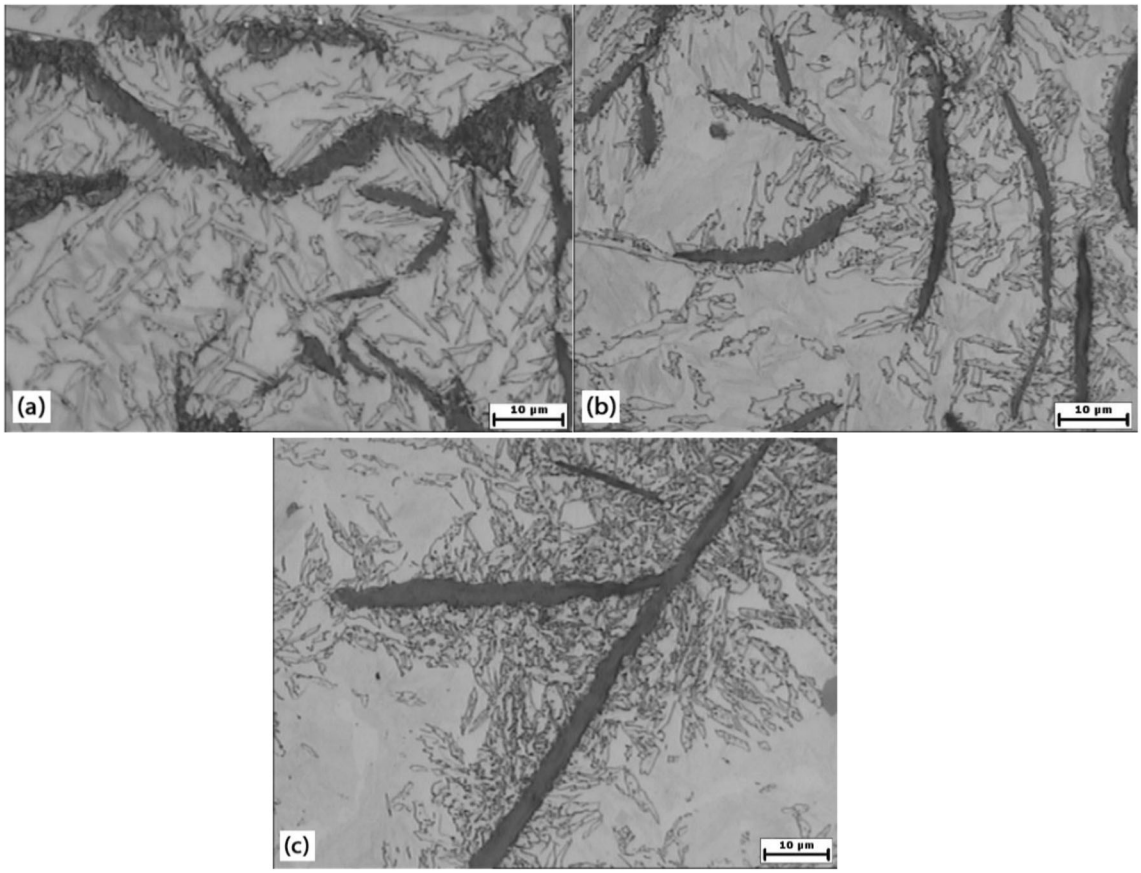

Fig. 6 Optical microscopy of 2% Nital etched specimens of rectangular cubic samples. (a) R-A with 380 °C, (b) R-B with 400 °C, (c) R-C with 420 °C as austempering temperatures

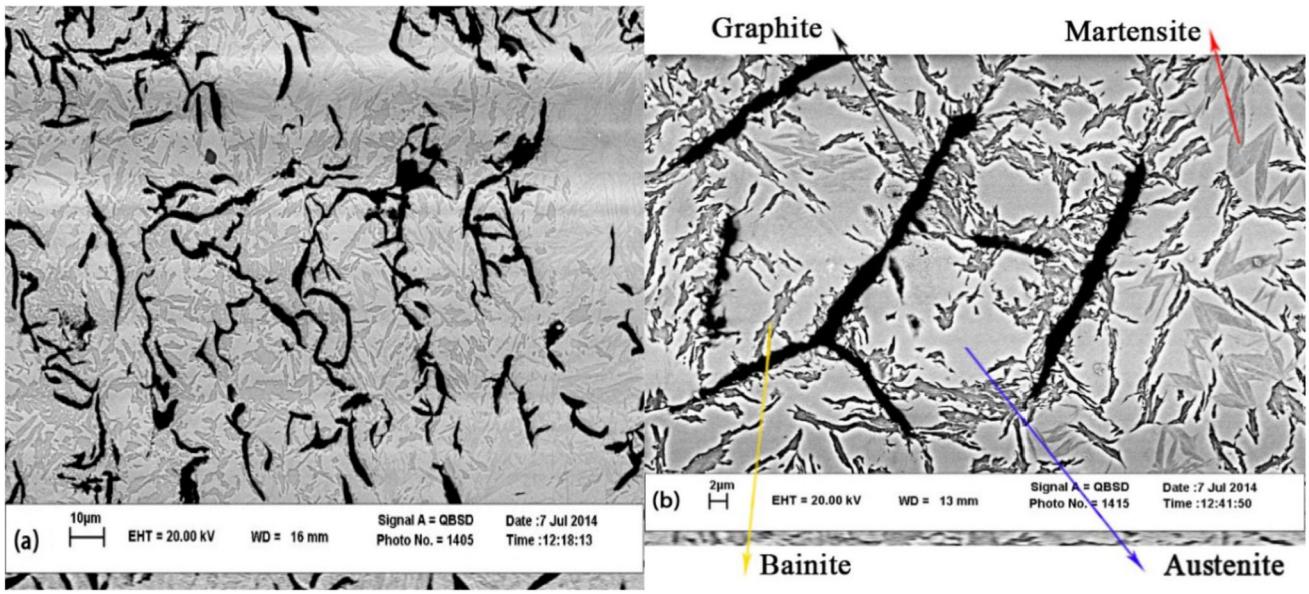

Fig. 7 SEM images of (a) B point in wedge-shaped sample, (b) R-A sample (color indication: black: graphite, yellow: bainitic ferrite, red: martensite, blue: austenite)

tunneling microscopy (STM) with reasonable interpretation based on following the former suggestions around topological features of bainitic ferrite adjacent to austenite (Ref 64), care approaching pattern accomplished to coincide imaging from these two phases in R-C as polished specimen and microstructure result and related topography illustrated in Fig. 8(a) and (b) after denoising.

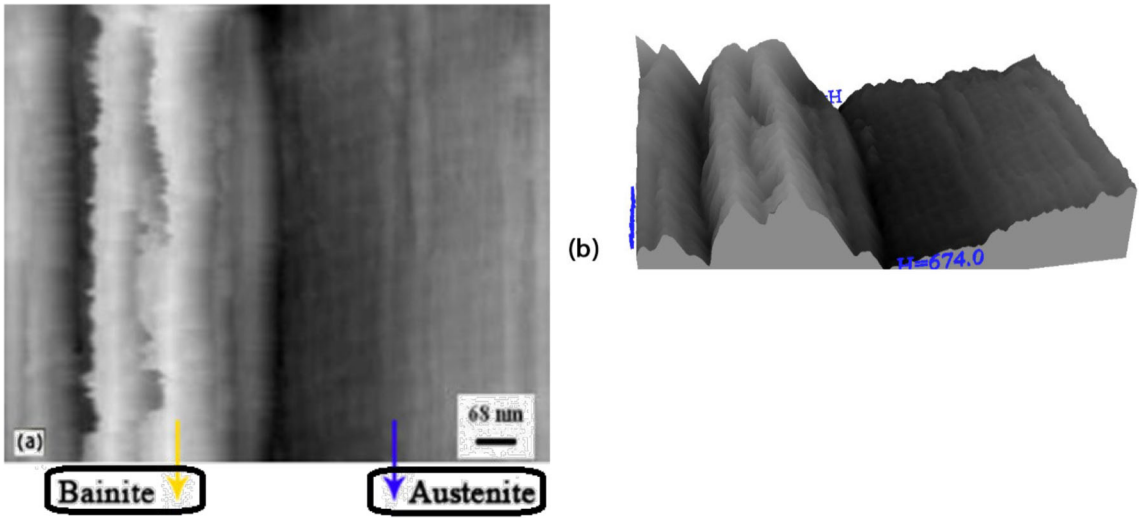

Fig. 8 (a-b) STM image of R-C sample austempered at 420 °C and related topography, respectively

Table 3 The result of the Charpy impact test and related standard deviation (SD)

Sample	Fracture energy, J/SD
R-A (380 °C)	3/0.5
R-B (400 °C)	4.5/1
R-C (420 °C)	5/1

3.2 Result of Impact Test

Table 3 shows the impact test results for rectangular cubic samples as a mean of four values for each austempering temperatures. To decrease the number of brittle properties as much as possible, the selected upper bainite region would be more efficient for investigation around impact test. Testing objects had a dimension of 55*10*10 mm, as described in ASTM A327 (Ref 66) for the unnotched Charpy impact test. Macroscopic examination of sample fracture surface confirms the brittle fracture of all samples. As shown in Table 3, a rough increase in impact toughness can be obtained by rising austempering temperature. Assuming the brittle nature of GCI, one may consider the Charpy impact toughness improvement as a result of higher fraction of bainitic ferrite and austenite phases in higher austempering temperature. It should be also noted that higher amount of austenite amidst the presence of graphite flakes of almost equal amount can cause highly dislocated bainite and devastation of impact toughness. But authors believe that lower fraction of martensite beside the higher amount of bainitic ferrite can cause the higher Charpy impact toughness by increasing austempering temperature.

3.3 Result of Hardness Test

An average for a minimum of three hardness indications was reported for each specimen. By this method, a general trend for hardness evolution in bulk material contains different microconstituent can be achieved. As can be seen, the higher austempering temperatures and lower cooling rates can bring the microstructure which is less hard. Table 4 illustrates hardness measurement in three points of austempered wedge-shaped specimens as already specified in Fig. 1. The table also consists of hardness measurements from the center point of rectangle samples with various austempering temperatures in the cross-sectional cut.

Table 4 Experimental hardness measurement for austempered wedge-shape and rectangular cubic samples and related standard deviation (SD)

Sample	Hardness (HV50), SD
Wedge-shaped A Point	262/3.3
Wedge-shaped B Point	271/2.4
Wedge-shaped C Point	285/0.6
R-A	277/2.3
R-B	258/1.9
R-C	235/4.5

Figure 10(a) indicates hardness values for simulated wedge-shaped sample in entire bulk and Figure 10(b) the cross-sectional cuts in x = 0, 25, and 63.5 mms (corner to the middle of sample) according to main parameters listed in Table 2 and Sect. 2.2. The figure also highlighted hardness variation along with the specified points by color intensity map. The surface section in x = 0 shows more substantial hardness characteristics and more rigid by hardness due to three different solid-chilling sides. By moving through the depth of the bulk sample causes a decreasing change in the hardness values, which is mainly dependent on distance to chilling sides and the amount of surrounded material to contribute to heat transfer. On the other hand, the melt just beneath of feeder can improve the heating of melt in y-axis of x = 63.5 mm. But the increasing trend in y-axis can be found by comparison between hardness color map in x = 63.5, 25, and 0 mms. Contact with higher amount of high-temperature melt is another reason for lower hardness of bulk material so close to feeder.

A comparative study was done for the Brinell hardness test for the wedge-shaped sample in the simulated as-cast model and the converted hardness results of Table 4 for the actual austempered condition of related samples. The results indicated in Fig. 10 are the hardness evolution during the z-direction,

which reports experimental hardness evaluation according to mentioned three z-points based on Fig. 1 and the same value for the z dimension of simulated condition at three different x values. A conversion table of ASTM E140 (Ref 66) was utilized to bring out Brinell hardness for all samples. Previous researchers confirmed the influence of high cooling rate in decreasing dendrite arm spacing (DAS) and secondary dendrite arm spacing (SDAS), which induce an increase in hardness value (Ref 8, 9). As shown in Fig. 9 and 10, there is a fluctuation in hardness measurement at the intervals from the vertex of simulated as-cast wedge-shaped samples to their basal planes. The maximum hardness relates to the apex, mainly containing a complex phase of carbides belonging to the probable white iron region. Along with the simulated sample, the minimum hardness measured at the A point, where the thick section size avoided a very high cooling rate caused to a smooth A-type graphite distribution as elaborated in previous sections. A significant increase in hardness value by austempering can be recognized from Table 4 and Fig. 10 but with fluctuation through wedge-shaped samples, which more validates the simulation trend. Figure 10 also confirms the result of past authors where they explored that austempering can increase hardness compared to the as-cast situation (Ref 38). The main reason for hardness variation through z direction could be the supporting role of bulk material in controlling the rate of chilling during solidification. It varies also in x direction where the samples use the benefit of chilling wall in cross-sectional cut of x = 0 mm in comparison with other sections. Based on results of Table 4 for rectangular cubic samples of R-A, R-B, and R-C, it can be concluded that the hardness amount decreased significantly by increasing austempering temperature. One reason could be increasing the austenite phase fraction and bainitic ferrite microconstituent fraction with improvement in the specific feather shape of upper bainite liked bainitic ferrite by subjecting samples to higher austempering temperatures. There is no doubt in the role of dislocation densities, material defects, and detachment affinity of graphite and matrix on elastic and plastic behavior of gray cast iron. However, as indicated in Table 3, higher austempering temperature in a constant time can cause lesser number of rigid phases like martensite and more austenite and bainitic ferrite fractions. It is more evident for R-C sample where the low amount of martensite can be form in comparison with other constituents. This issue is already explained in Sect. 3.1 and would be the main reason for supposed higher Charpy impact toughness form 380-420 C austempering temperature.

4. Conclusions

This study focused on an examination of low-alloyed gray cast iron (GCI) containing nickel (Ni) and molybdenum (Mo) elements, investigating the impact of bainite heat treatment at different austempering temperatures on microstructural features and mechanical properties. Rectangular cubic and wedge-shaped samples were utilized, showcasing varying section sizes to elucidate their influence on microstructure.

The findings of this research have yielded several critical insights:

The transition in graphite morphology from Type A to a combination of Types D and E with decreasing section size is attributed to intensified cooling rates in thinner sections.

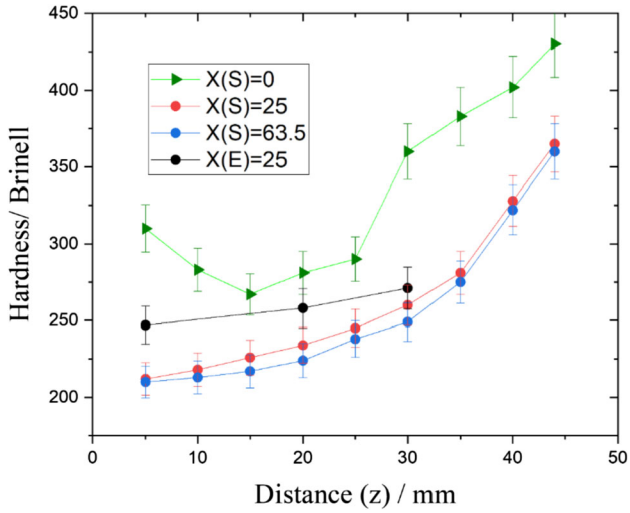

Fig. 10 Comparison hardness in simulated as-cast and austempered wedge-shaped samples. (S: simulation and E: experimental) all x and z dimensions are mm (± 2)

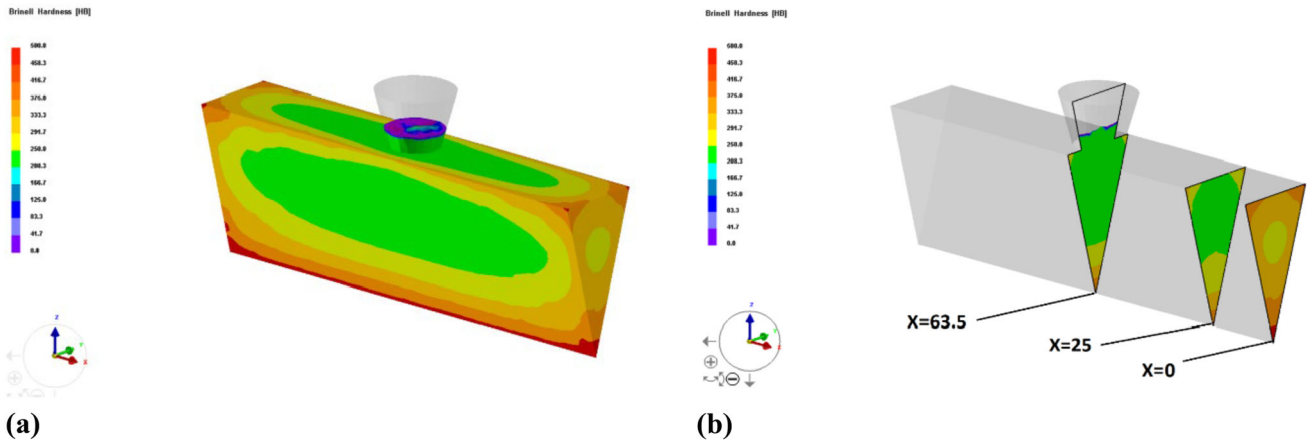

Fig. 9 Hardness map for simulated wedge-shaped sample in as-cast condition, (a) bulk sample and (b) cross-sectional cut in x = 0, 25, and 63.5 mms

Higher cooling rates in thinner sections result in increased martensite phases and precipitated carbides, contributing significantly to augmented hardness.

Scanning tunneling microscopy analysis revealed a distinctive tent-like topology in the bainitic ferrite microstructure, providing insights into the deformation characteristics of austenite during the transformation.

Elevated austempering temperatures affected the upper bainite shape bainitic ferrite, resulting in coarsening of the microstructure and influencing impact energy absorption and hardness values.

The austempering process proved effective in enhancing hardness compared to the as-cast state, attributable to the complex contribution of various phases.

These findings hold paramount importance for both researchers and industrial practitioners, guiding future endeavors in the design of heat treatments for GCI to attain desired mechanical properties. The optimization of microstructure through refined heat treatment processes can significantly enhance the performance and reliability of GCI components, further warranting continued exploration and advancement in this domain.

Acknowledgments

The authors would like to thank the Faculty of Engineering of Ferdowsi University in Mashhad and the School of Materials Science and Engineering of Tsinghua University for supporting the implementation of this study. The first author is also profoundly thankful to Prof. Hao Chen for his deep affection perseverance in improving his critical thinking attitude.

Authors Contribution

Kamran Kaboli helped in conceptualization, methodology, formal analysis, investigation, writing and editing—original draft. Meisam Mostafapour, N. Kheirkhahan, E. Edalati were involved in formal analysis and investigation. E. Solbi helped in simulation. A. Babakhani supervised the study. A.R. Kiani-Rashid contributed to conceptualization, supervision, project administration, resources.

Funding

No funding.**Availability of Data and Material**

The data that support the results of this study are available from the corresponding author upon request.

Code Availability

Not applicable.

Conflict of interest

The authors declare that they do not have any competing financial interests/personal associations that may influence the work reported in this paper.

References

1. Census of World Casting Production: Global Casting Production Growth Stalls, December 2021, Modern Casting Magazine. 1695 North Penny Lane, Schaumburg, IL 60173 American Foundry Society. **111**, p 26–27
2. B. Kovacs, On the Terminology and Structure of ADI, *AFS Trans.*, 1994, **102**, p 417–420
3. H.K.D.H. Bhadeshia, *Bainite in Steels: Theory and Practice*, 3rd ed. CRC Press, London, 2015. https://doi.org/10.1201/9781315096674
4. H.T. Angus, *Cast Iron: Physical and Engineering Properties*, 2nd ed. UK7 Butterworth, 1976. https://doi.org/10.1016/C2013-0-01035-3
5. K. Aliakbari, Failure Analysis of Ductile Iron Crankshaft in Four-Cylinder Diesel Engine, *Int. Metalcast.*, 2021, **15**, p 1223–1237. https://doi.org/10.1007/s40962-020-00550-y
6. R. Singh, *7 - Cast Iron and Cast Steel*, 3rd ed. Butterworth-Heinemann, 2020, p 61–76. https://doi.org/10.1016/B978-0-12-821348-3.00020-3
7. G.I. Sil'man, *Metallov. Term. Obrab. Met.*, 2002, (1), p 26–29. (https://www.sciencedirect.com/science/article/pii/B9780128213483000203)
8. M.M. Jabbari Behnam, P. Davami, and N. Varahram, Effect of Cooling Rate On Microstructure and Mechanical Properties of Gray Cast Iron, *Mater. Sci. Eng. A*, 2010, **528**(2), p 583–588. https://doi.org/10.1016/j.msea.2010.09.087
9. L. Ji, X. Du, Y. Sun et al., Effect of Solidification Rate on Microstructure and Mechanical Characteristic of Gray Cast Iron, *Int. Metalcast.*, 2023 https://doi.org/10.1007/s40962-023-01082-x
10. S.K. Shaha and M.M. Haque, Simulation of Heat Flow in Computational Method and its Verification on the Structure and Property of Gray cast iron, *Am. J. Appl. Sci.*, 2010, **7**, p 795–799. https://doi.org/10.3844/ajassp.2010.795.799
11. ASTM A247-10, Standard Test Method for Evaluating the Microstructure of Graphite in Iron Castings, https://doi.org/10.1520/A0247-19, www.astm.org
12. P. Ferro, T. Borsato, F. Bonollo, and S. Pavodan, A Solidification Time-Based Method for Rapid Evaluation of the Mechanical Properties of Gray Iron Castings, *Int. Metalcast.*, 2019, **13**, p 845–852. https://doi.org/10.1007/s40962-018-0290-8
13. S. Pal, Correlation Between Solidification Time and Cooling Rate, Microstructure and Tensile Strength of a Low Alloyed Grey Cast Iron, *Mater. Sci. Forum*, 2018, **925**, p 257–263. https://doi.org/10.4028/www.scientific.net/MSF.925.257
14. A.R. Kiani-Rashid, M. Mostafapour, S.K. Kaboli-Mallak, and A. Babakhani, The Effect of Cooling Rate on Bainite Phase Formation in Austempered Nickel-Molybdenum Gray Cast Iron, *ISRN Mater. Sci.*, 2011 https://doi.org/10.5402/2011/923241
15. S. Sahu, M.N. Bhat, A. Kumar, A. Pratik, and A. Kumar, Effect of Section Thickness on the Microstructure and Hardness of Gray Cast Iron (A Simulation Study), *Int. J. Eng. Res. Technol*, 2014, **3**, p 35–41. https://doi.org/10.3390/met7120549
16. L. Collini, G. Nicoletto, and R. Konečná, Microstructure and Mechanical Properties of Pearlitic Gray Cast Iron, *Mater. Sci. Eng. A*, 2008, **488**(1–2), p 529–539. https://doi.org/10.1016/j.msea.2007.11.070
17. C.H. Hsu, Y.H. Yu, and S.C. Lee, Effect of Austempering Heat Treatment on Fracture Toughness of Copper Alloyed Gray Iron, *Mater. Chem. Phys.*, 2000, **63**, p 75–81. https://doi.org/10.1016/S0254-0584(99)00213-8
18. B. Wang, G.C. Barber, F. Qiu, Q. Zou, and H. Yang, A Review: Phase Transformation and Wear Mechanisms of Single-Step and Dual-Step Austempered Ductile Irons, *J. Mater. Res. Technol.*, 2020, **9**, p 1054–1069. https://doi.org/10.1016/j.jmrt.2019.10.074
19. H. Bayati and R. Elliott, Austempering Process in High Manganese Alloyed Ductile Cast Iron, *Mater. Sci. Technol.*, 1995, **11**, p 118–129. https://doi.org/10.1179/mst.1995.11.2.118
20. I. Chakrabarty, Heat Treatment of Cast Irons, *Comprehensive Materials Finishing*. M.S.J. Hashmi Ed., Elsevier, Amsterdam, 2017, p 246–287
21. H.R. Erfanian-Naziftoosi, N. Haghdadi, and A.R. Kiani-Rashid, the Effect of Isothermal Heat Treatment Time on the Microstructure and Properties of 2.11% Al Austempered Ductile Iron, *J. Mater. Eng. Perform.*, 2012, **21**(8), p 1785–1792. https://doi.org/10.1007/s11665-011-0086-y
22. A.R. Kiani-Rashid, The Bainite Transformation and the Carbide Precipitation of 4.88% Aluminium Austempered Ductile Iron Inves-

tigated Using Electron Microscopy, *J. Alloys Compd.*, 2009, **474**(1–2), p 490–498. https://doi.org/10.1016/j.jallcom.2008.06.131
23. B.V. Kovacs and J.R. Keough, Physical Properties and Application of Austempered Gray Iron, *AFS Trans.*, 1993, **101**, p 283–291
24. K.B. Rundman, J.R. Parolini, and D.J. Moore, Relationship Between Tensile Properties and Matrix Microstructure in Austempered Gray Iron, *AFS Trans.*, 2005, **113**, p 723–737
25. D.J. Moore, J.R. Parolini, and K.B. Rundman, On the Kinetics of Austempered Gray Cast Iron, *AFS Trans.*, 2003, **111**, p 911–930
26. K. Hayrynen, D. Moore, J. Parolini, and K. Rundman, On the Thermal Stability of Ausferrite in Austempered Gray Iron Components for Long Exposure High-Temperature Applications, *AFS Trans.*, 2006, **114**, p 627–635
27. T. Sarkar and G. Sutradhar, Relationship Between Matrix-Microstructure and Mechanical Properties of Copper Alloyed Thin Wall Austempered Gray Cast Iron (TWAGI), *Int. J. Cast Met. Res.*, 2018, **31**, p 20–28. https://doi.org/10.1080/13640461.2017.1351705
28. A.H. Seikh, A. Sarkar, J.K. Singh, S.M.A. Khan, N.A. Mohammed, and M. Ghosh, Corrosion Characteristics of Copper-Added Austempered Gray Cast Iron (AGCI), *Materials*, 2019, **12**(3), p 503. https://doi.org/10.3390/ma12030503
29. G. Balachandran, A. Vadiraj, M. Kamaraj, and E. Kazuya, Mechanical and Wear Behavior of Alloyed Gray Cast Iron in the Quenched and Tempered and Austempered Conditions, *Mater. Des.*, 2011, **32**, p 4042–4049. https://doi.org/10.1016/j.matdes.2011.03.054
30. B. Wang, Y. Pan, Y. Liu, G.C. Barber, F. Qiu, and M. Hu, Wear Behavior of Composite Strengthened Gray Cast Iron by Austempering and Laser Hardening Treatment, *J. Mater. Res. Technol.*, 2020, **9**, p 2037–2043. https://doi.org/10.1016/j.jmrt.2019.12.036
31. T. Sarkar and G. Sutradhar, Tribological Characterization of Copper Alloyed Austempered Gray Cast Iron (AGI), *Mater. Res. Express*, 2018, **5**(6), p 066542. https://doi.org/10.1088/2053-1591/aacc86
32. S. Sharma and A. Hegde, An Analysis of the Amount of Retained Austenite in Manganese Alloyed Austempered Ductile Iron, *Mater. Res.*, 2021 https://doi.org/10.1590/1980-5373-mr-2021-0301
33. B. Shakeri, E. Heidari, and S.M.A. Boutorabi, Effect of Isothermal Heat Treatment Time on the Microstructure and Properties of 4.3% Al Austempered Ductile Iron, *Int. J. Metalcast.*, 2023, **17**(4), p 3005–3018. https://doi.org/10.1007/s40962-023-00980-4
34. M. Jimenez-Martinez and M. Alfaro-Ponce, Effects of Synthetic Data Applied to Artificial Neural Networks for Fatigue Life Prediction in Nodular Cast Iron, *J. Brazil. Soc. Mech. Sci. Eng.*, 2021, **43**(1), p 10. https://doi.org/10.1007/s40430-020-02747-y
35. A.M. Aziz, M.Z. Omar, S. Samat, I.F. Mohamed, M.A. Aripin, and M.R. Mazlan, Microstructural Characterisation and High-cycle Fatigue Behaviour of Semisolid Al-Si-Cu Alloy, *Int. Metalcast.*, 2023, **18**(3), p 2612–2623. https://doi.org/10.1007/s40962-023-01194-4
36. M.M. Ibrahim, A.M. Negm, S.S. Mohamed et al., Fatigue Properties and Simulation of Thin Wall ADI and IADI Castings, *Int. Metalcast.*, 2022, **16**, p 1693–1708. https://doi.org/10.1007/s40962-021-00711-7
37. A. Uyar, O. Sahin, B. Nalcaci et al., Effect of Austempering Times on the Microstructures and Mechanical Properties of Dual-Matrix Structure Austempered Ductile Iron (DMS-ADI), *Int. Metalcast.*, 2022, **16**, p 407–418. https://doi.org/10.1007/s40962-021-00617-4
38. F.H. Çakir, The Effect of Cryogenic Treatment on Hardness, Toughness, and Tribological Properties of Austempered Ductile Iron with Different Nickel Contents, *Int. Metalcast.*, 2021 https://doi.org/10.1007/s40962-021-00686-5
39. D.O. Fernandino, M.G. López, R.E. Boeri et al., Influence of Microshrinkage Cavities on the Plastic Deformation and Fracture Under Tensile Loading in Ferritic Ductile Iron, *Int. Metalcast.*, 2021, **15**, p 1084–1090. https://doi.org/10.1007/s40962-020-00546-8
40. G. Artola, I. Gallastegi, J. Izaga et al., Austempered Ductile Iron (ADI) Alternative Material for High-Performance Applications, *Int. Metalcast.*, 2017, **11**, p 131–135. https://doi.org/10.1007/s40962-016-0085-8
41. S.E. Kisakurek and A. Ozel, Unnotched Charpy Impact Energy Transition Behavior of Austempered Engineering Grade Ductile Iron Castings, *Metall. Mater. Trans. B*, 2014, **45**, p 454–463. https://doi.org/10.1007/s11663-013-9976-8
42. T. Sarkar and G. Sutradhar, Influence of Austenitizing Temperature on Microstructure and Mechanical Properties of Austempered Gray Iron (AGI), *Mater. Today Proc.*, 2017, **4**, p 10138–10143. https://doi.org/10.1016/j.matpr.2017.06.336
43. R. Gundlach, M. Meyer, and L. Winardi, Influence of Mn and S on the Properties of Cast Iron Part III—Testing and Analysis, *Int. Metalcast.*, 2015, **9**, p 69–82. https://doi.org/10.1007/BF03355617
44. P.A. Blackmore and R.A. Harding, The Effects of Metallurgical Process Variables on the Properties of Austempered Ductile Irons, *J. Heat Treating*, 1984, **3**, p 310–325. https://doi.org/10.1007/BF02833125
45. T. Tokunaga, Y.-J. Kim, and H. Era, Effect of Nickel Content on Microstructural Evolution in Austempered Solution-Strengthened Ferritic Ductile Cast Iron, *J. Mater. Eng. Perform.*, 2019, **28**(7), p 4034–4040. https://doi.org/10.1007/s11665-019-04184-y
46. P. Sellamuthu, D.G.H. Samuel, D. Dinakaran, V.P. Premkumar, Z. Li, and S. Seetharaman, Effect of Nickel Content and Austempering Temperature on Microstructure and Mechanical Properties of Austempered Ductile Iron (ADI), *IOP Conf. Ser. Mater. Sci. Eng.*, 2018, **383**, 012069. https://doi.org/10.1088/1757-899X/383/1/012069
47. K.L. Hayrynen, J.R. Keough, and B.V. Kovacs, The Effects of Alloying Elements on the Critical Temperatures in Ductile Iron. Ductile Iron Society, Research Report No. 22. 1997
48. ASTM A367-11, Standard Test Methods for Chill Testing of Cast Iron, https://doi.org/10.1520/A0367-22, www.astm.org
49. Y. Pan, B. Wang, X. Han et al., Study of Transformation Kinetics for Austempered Gray Cast Iron, *Phys. Metals Metallogr.*, 2020, **121**, p 1249–1257. https://doi.org/10.1134/S0031918X20130153
50. ASTM E3-11, Standard Guide for Preparation of Metallographic Specimens. https://doi.org/10.1520/E0003-11R17, www.astm.org
51. ASTM A327-11, Standard Test Methods for Impact Testing of Cast Irons. https://doi.org/10.1520/A0327_A0327M-22, www.astm.org
52. M. Kazemi, A.R. Kiani-Rashid, and A. Nourian, Impact Toughness and Microstructure of Continuous Medium Carbon Steel Bar-Reinforced Cast Iron Composite, *Mater. Sci. Eng. A*, 2013, **559**, p 135–138. https://doi.org/10.1016/j.msea.2012.08.051
53. A. Diószegi and I.L. Svensson, On the Problems of Thermal Analysis of Solidification, *Mater. Sci. Eng. A*, 2005, **413–414**, p 474–479. https://doi.org/10.1016/j.msea.2005.09.052
54. A. Diószegi and J. Hattel, Inverse Thermal Analysis Method to Study Solidification in Cast Iron, *Int. J. Cast Metals Res.*, 2004, **17**, p 311–318. https://doi.org/10.1179/136404604225020687
55. E. Fraś, W. Kapturkiewicz, and H.F. Lopez, The Solidification Kinetics of Cast Iron using an Improved Thermal Analysis Technique, *Cast Metals*, 1993, **6**, p 137–142. https://doi.org/10.1080/09534962.1993.11819139
56. S. Sulaiman and A.M.S. Hamouda, Modeling of the Thermal History of the Sand-Casting Process, *J. Mater. Process. Technol.*, 2001, **113**, p 245–250. https://doi.org/10.1016/S0924-0136(01)00592-1
57. D. Sundaram, The Effect of Solidification time and Cooling rate on the Ultimate tensile Strength of Gray Cast Iron. [Internet] [Dissertation]. 2018, Available from: http://urn.kb.se/resolve?urn=urn:nbn:se:kth:diva-238856
58. S.K. Kaboli-Mallak, N. Kheirkhahan, E. Edalati et al., On the Morphology Variation of Graphite in Ductile Cast Iron through Severe Plastic Deformation, *Phys. Metals Metallogr.*, 2023, **124**, p 1813–1825. https://doi.org/10.1134/S0031918X23601312
59. S. Seidu and L.O. Otunniyi, Control of Chilling Tendency in Gray Cast Iron Reuse, *Mater. Res.*, 2013, **16**, p 145–149. https://doi.org/10.1590/S1516-14392012005000160
60. E. Fraś, H.F. Lopez, M. Kawalec, and M. Gorny, Role of Alloying Additions in the Solidification Kinetics and Resultant Chilling Tendency and Chill of Cast Iron, *Metals*, 2015, **5**, p 256–288. https://doi.org/10.3390/met5010256
61. Z. Ławrynowicz, Kinetics of the Bainite Transformation in Austempered Ductile Iron ADI, *Adv. Mater. Sci.*, 2016, **16**(2), p 47–56. https://doi.org/10.1515/adms-2016-0008
62. L.C. Chang, Carbon Content of Austenite in Austempered Ductile Iron, *Scripta Mater.*, 1998, **39**(1), p 35–38. https://doi.org/10.1016/S1359-6462(98)00132-8
63. X. Wang, D. Yuzhou, C. Liu, H. Zhitao, P. Li, Z. Gao, H. Guo, and B. Jiang, Relationship Among Process Parameters, Microstructure, and Mechanical Properties of Austempered Ductile Iron (ADI), *Mater. Sci. Eng. A*, 2022, **857**, p 144063. https://doi.org/10.1016/j.msea.2022.144063
64. Z.-G. Yang and H.-S. Fang, An overview on Bainite Formation in Steels, *Curr. Opin. Solid State Mater. Sci.*, 2005, **9**(6), p 277–286. https://doi.org/10.1016/j.cossms.2006.06.005

65. L.C.D. Fielding, The Bainite Controversy, *Mater. Sci. Technol.*, 2013, **29**(4), p 383–399. https://doi.org/10.1179/1743284712Y.0000000157
66. ASTM E140-19, Standard Hardness Conversion Tables for Metals Relationship among Brinell hardness, Vickers Hardness, Rockwell Hardness, Superficial Hardness, Knoop Hardness, Scleroscope Hardness, and Leeb Hardness. https://doi.org/10.1520/E0140-12BR19E01